Construction of heterostructured CuFe$_2$O$_4$/g-C$_3$N$_4$ nanocomposite as an efficient visible light photocatalyst with peroxydisulfate for the organic oxidation

Ruobai Li[a], Meixuan Cai[a], Zhijie Xie[a], Qianxin Zhang[a], Yongqin Zeng[a], Haijin Liu[b], Guoguang Liu[a,*], Wenying Lv[a]

[a] School of Environmental Science and Engineering, Guangdong University of Technology, Guangzhou 510006, China
[b] School of Environment, Henan Normal University, Henan Key laboratory for Environmental Pollution Control, Xinxiang 453007, China

ABSTRACT

A copper ferrite modified graphitic carbon nitride (CuFe$_2$O$_4$/g-C$_3$N$_4$) nanocomposite was successfully synthesized for the utilization as a visible-light responsive photocatalyst. The as-synthesized catalysts were characterized using X-ray diffraction (XRD), Fourier transform infrared spectroscopy (FTIR), scanning electron microscopy (SEM), transmission electron microscopy (TEM), X-ray photoelectron spectroscopy (XPS), UV–vis diffuse reflectance spectra (UV–vis/DRS), photoluminescence (PL) analysis, and an electrochemical workstation. Compared to g-C$_3$N$_4$ and CuFe$_2$O$_4$, the CuFe$_2$O$_4$/g-C$_3$N$_4$ composites possessed excellent photocatalytic performance for the destruction of propranolol (PRO). A removal efficiency of 82.2% was achieved with 1 g/L catalyst and 1 mM peroxydisulfate (PDS) under visible light irradiation (λ < 420 nm) within 120 min. The g-C$_3$N$_4$ coupled with CuFe$_2$O$_4$ improved the capacity for visible light capture, whereas the presence of PDS enhanced the transfer of photogenerated electron. Quenching experiments and electron spin resonance (ESR) suggested that the reactive oxygen species (ROS) were superoxide radicals (O$_2^{\cdot-}$), h$^+$, hydroxyl radicals ($\cdot$OH), and sulfate radicals (SO$_4^{\cdot-}$). Moreover, the byproducts of PRO were investigated by HPLC-MS/MS, and the transformation pathways under the Vis/g-C$_3$N$_4$/CuFe$_2$O$_4$/PDS process were tentatively proposed based on the intermediates. The research provided a potential approach of CuFe$_2$O$_4$ modified g-C$_3$N$_4$ as a photocatalyst combined with PDS for the treatment of contaminated water.

1. Introduction

Beta (β)-blockers comprise a specific classification of drugs that have been widely applied for the treatment of various cardiovascular diseases. However, these drugs may be released through hospital effluents and industrial pharmaceutical waste streams. Since conventional wastewater treatment plant (WWTP) processes do not have the ability to remove these drugs efficiently, they are released into ambient aqueous environments [1]. These compounds and their metabolites have been frequently detected in the aquatic environment, or even in groundwater at concentrations that range from ng/L to μg/L [2]. And the widespread occurrence of β-blockers can impart potential damage to aquatic organisms [3]. As one of most common β-blockers, propranolol (PRO) possesses a relatively higher acute and chronic toxicity, and due to its persistence may have potentially adverse effects on ecosystems. Several studies have reported the potential toxic effects of PRO on

fish, crustaceans, and green algae [4]. It should be noted that conventional wastewater treatment via the application of activated sludge is not effective for the complete elimination of propranolol. Hence, it is necessary to develop effective treatment technologies for the removal of PRO in the aquatic environments.

Advanced oxidation processes (AOPs) constitute a promising technology for the destruction of organic contaminants through the generation of highly reactive radical species [5]. AOPs derived from a combination of technologies including UV/H$_2$O$_2$ [6], photoelectron-Fenton [7], UV/O$_3$, and O$_3$/H$_2$O$_2$ [8], have been frequently applied for the destruction of PRO. However, these homogeneous processes suffer from the drawbacks such as the harsh reactive conditions, relatively complicated operations and high cost. In consideration of the sustainable energy from the sun, photocatalysis through the efficient utilization of solar energy has been considered to be one of the most advantageous strategies for the removal of organic contaminants [9]. The

exploration of suitable photocatalysts for the effective removal of PRO under solar irradiation has garnered tremendous attention.

As a metal-free photocatalyst with a p-conjugated structure, graphitic carbon nitride (g-C_3N_4) has great potential for the destruction of organic compounds under visible light. This photocatalyst possesses a narrow band gap of approximately 2.7 eV, which has capacity to harvest the solar spectrum [10]. However, low specific surface area, the limited delocalized conductivity, and high photogenerated electron-hole pair recombination rate of g-C_3N_4 materials has resulted in unsatisfactory photocatalytic efficiencies [11]. Many attempts have been made to overcome the limitations of g-C_3N_4, including morphological control, metal and non-metal doping, and coupling with other semiconductors to form p-n heterojunctions [12,13]. Heterojunctions based on g-C_3N_4 encompassing TiO_2/g-C_3N_4 [14], CdS/g-C_3N_4 [15], ZnO/C_3N_4 [16], WO_3/g-C_3N_4 [17], and BiOX-g-C_3N_4 [18,19] have been employed to enhance light absorption as well as photogenerated electron-hole pair separation.

Spinel ferrites, MFe_2O_4 (M = Mn, Fe, Co, Ni, Cu, Zn), have recently attracted tremendous attention in catalysis owing to their environmental compatibility and stability as well as their easy synthesis. A p-type semiconductor referred to as $CuFe_2O_4$, with a relatively narrow band gap of 1.4 eV, has been applied in various fields, particularly in electronics and catalysis [20,21]. The combination of $CuFe_2O_4$ with g-C_3N_4 provides a convenient and cost-effective strategy for the magnetic separation of photocatalysts due to its high electromagnetic performance. It has been anticipated that $CuFe_2O_4$ coupled with g-C_3N_4 to form p-n heterojunctions can enhance the efficacy of photoinduced charge separation under visible light irradiation due to their perfect matching between the conduction band (CB) and valence band (VB). Meanwhile, peroxydisulfate (PDS) might be activated by $CuFe_2O_4$ and the photogenerated electrons to form $SO_4^{\cdot-}$, which further improves the synergistic photocatalytic performance of $CuFe_2O_4$ and g-C_3N_4. It's established that $SO_4^{\cdot-}$ possesses stronger oxidizing capability and higher selectivity contrast to $\cdot OH$ for the oxidation of organic compounds [22].

In this work, we report on the photocatalytic degradation of propranolol over $CuFe_2O_4$/g-C_3N_4 heterojunctions under visible light irradiation. To accelerate the photocatalytic performance of $CuFe_2O_4$/g-C_3N_4 for the eradication of propranolol, peroxydisulfate was incorporated into the system as an electron acceptor. The physical and chemical characterization of the $CuFe_2O_4$/g-C_3N_4 heterojunction was carried out. The effects of several critical factors (e.g., catalyst and peroxydisulfate doses) in terms of its photocatalytic activity were also investigated. The reactive species responsible for the photocatalytic process were identified by quenching experiments and electron spin resonance (ESR). Finally, the intermediates generated under Vis/$CuFe_2O_4$/g-C_3N_4/peroxydisulfate system were determined by LC–MS/MS, and the transformation pathways were tentatively proposed.

2. Experimental

2.1. Materials

Propranolol hydrochloride (99%), 5,5-dimethyl-1-pyrroline N-oxide (DMPO), and 4-oxo-2,2,6,6-tetramethylpiperidine (TEMP) were obtained from Sigma–Aldrich (USA). Benzoquinone (BQ) was purchased from J&K Scientific Ltd. Sodium oxalate ($Na_2C_2O_4$), citric acid, copper nitrate ($Cu(NO_3)_2.3H_2O$), ferric nitrate ($Fe(NO_3)_3.9H_2O$) and peroxydisulfate (PDS) were purchased from Aladdin Reagent Co., Ltd. (Shanghai, China). $K_2Cr_2O_7$ was purchased from Sinopharm Chemical Reagent (Shanghai, China). Ethanol (EtOH) and tert-butyl alcohol (TBA) were obtained from Guangzhou Chemical Reagent Factory (China). All reagents used were of analytical grade, without further purification. Ultrapure water (resistance > 18.25 MΩ) was provided by a water purification system (TKA, Germany).

2.2. Synthesis of g-C_3N_4/$CuFe_2O_4$ samples

The g-C_3N_4 was synthesized through calcination with a dicyandiamide precursor [23]. Typically, 4 g dicyandiamide was introduced into a ceramic crucible, and then placed in a muffle furnace at 550 °C using a heating rate of 5 °C min^{-1} for 4 h.

$CuFe_2O_4$ magnetic nanoparticles (MNPs) were prepared via a sol-gel combustion method [24]. Typically, 0.005 mol $Cu(NO_3)_2 \cdot 3H_2O$ and 0.01 mol $Fe(NO_3)_3 \cdot 9H_2O$ were dissolved in an aqueous solution and stirred at 60 °C for 2 h, to which 0.015 mol citric acid was added to attain unity. The resultant homogeneous solution was stirred for an additional 2 h at 60 °C, and then placed in an 80 °C water bath to evaporate the water. The obtained resultant was transferred to a muffle furnace at 400 °C for 2 h to remove the citric acid and obtain a fine oxide powder.

Different quantities of g-C_3N_4 and $CuFe_2O_4$ were dispersed in 15 ml ethanol and 15 ml ultrapure water in an alumina crucible, which was ultrasonicated for 30 min, and then heated in water bath under continuous stirring at 80 °C to evaporate the solvents. Subsequently, the mixture was placed in a muffle furnace for 2 h at 300 °C after which the products were cooled to room temperature. The resulting product was rinsed with distilled water, and dried under vacuum oven at 60 °C for 12 h to obtain the g-C_3N_4 coupled with $CuFe_2O_4$; denoted as a g-C_3N_4/$CuFe_2O_4$ heterojunction with different mass ratios.

2.3. Characterization

The XRD patterns were recorded using a Rigaku Ultimate IV diffractometer under Cu Kα radiation (10° min^{-1} from 10 to 80°). Fourier transform infrared (FTIR) spectra were obtained using a Nicolet FTIR 6700 spectrometer to identify the photocatalytic functional groups. The morphologies of the samples were characterized through scanning electron microscopy (SEM) with a Hitachi S4800. Transmission electron microscopy (TEM) was performed with a JEM-2100 F to investigate the crystal planes and fringes of the samples. X-ray photoelectron spectroscopy (XPS) was examined through an ESCALAB 250XI (Thermo Scientific) to analyze the electronic states of the surface. The UV–vis diffuse reflectance spectra (UV–vis DRS) of the samples were conducted using a UV-2550, Shimadzu UV–vis spectrometer. The photoluminescence (PL) spectra of the samples were obtained with a FS5 fluorescence spectrometer.

The transient photocurrent measurements and electrochemical impedance spectroscopy (EIS) were performed using a CHI660E electrochemical analyzer, which were measured via a three-electrode system with a saturated calomel electrode (SCE) as the reference electrode. Detailed operational conditions are presented in the Supplementary data, Text S1.

2.4. Photocatalytic experiment

The photocatalytic activity of the g-C_3N_4/$CuFe_2O_4$ was quantified in a photoreactor (XPA-7, Nanjing XUJ Co. Ltd.) with a cylindrical quartz tube. A 350 W Xenon lamp with an UV cut-off filter (λ > 420 nm) was employed as a visible light source. The schematic diagram of the experimental setup is displayed in Fig. S1. For each experiment, 50 mL of a 0.02 mM PRO aqueous solution was transferred into the photoreactor, where the pH was maintained at its initial state. Certain quantities of the g-C_3N_4/$CuFe_2O_4$ samples were added to the reactor under continuous stirring for 30 min. to achieve the adsorption equilibrium (under dark conditions). Subsequently, predetermined quantities of the PDS were introduced into the photoreactor, and the Xenon lamps were switched on. At specific time intervals, 1 mL samples were extracted from the suspension during irradiation. The concentration was quantified by high performance liquid chromatography (HPLC) analysis.

2.5. Detection of reactive radicals

To detect the reactive radicals that were generated during the photocatalytic reaction, tert-butyl alcohol) (TBA), sodium oxalate ($Na_2C_2O_4$), benzoquinone (BQ), and potassium dichromate ($K_2Cr_2O_7$) were added to the PRO solution that contained the g-C_3N_4/$CuFe_2O_4$ composite photocatalyst to trap sulfate radicals ($SO_4^{\cdot-}$), superoxide radicals ($O_2^{\cdot-}$), holes (h^+), and e^-, respectively. Furthermore, ethanol (EtOH) was also added to the photocatalytic reaction system to quench both hydroxyl radicals (•OH) and sulfate radicals ($SO_4^{\cdot-}$). The electron spin resonance (ESR) signals of the radicals were captured by 5,5-dimethyl-1-pyrroline-N-oxide (DMPO) to detect $\cdot$OH, $SO_4^{\cdot-}$, and $O_2\bullet^-$, while 4-oxo-2, 2, 6, 6-tetramethylpiperidine (TEMP) was employed for the detection of $^1O_2$. The reactive radicals responsible for the photocatalytic process were detected using a Bruker model ESR JES-FA200 spectrometer.

2.6. Detection of PRO concentration and byproducts

The concentrations of the PRO solutions were determined using a high-performance liquid chromatography (HPLC) instrument (Waters, USA), which consisted of a Hypersil C18 column (250 × 4.6 mm, 5 μm). The mobile phase of PRO contained 30% methanol (HPLC-grade) and a 70% acetic acid solution (formic acid, 0.2%). The flow rate was 1 mL·min^{-1} and the detection wavelength was set at 213 nm.

The degradation byproducts were detected using a HRAM LC/MS/MS, which consisted of a HPLC system (Ultimate 3000RSLC, Thermo Scientific, USA) and a Q Exactive Orbitrap mass spectrometer. A Hypersil GOLD C18 (100 × 2.1 mm, 1.9 μm) was employed to separate the byproducts. Details of the mobile phase composition and gradient elution are presented in Table S1.

The detailed operational conditions of the HRAM LC/MS/MS are shown in Tables S2 and S3.

3. Results and discussion

3.1. Structure and morphological analysis

Fig.1a reveals the XRD patterns of the $CuFe_2O_4$/g-C_3N_4 photocatalysts that contained various quantities g-C_3N_4, together with pure g-C_3N_4 and $CuFe_2O_4$. The XRD pattern of the $CuFe_2O_4$ presented three intense diffraction 2θ angles at 30.2°, 35.4°, and 62.8°, corresponding to the (220), (311), and (440) planes of the tetragonal $CuFe_2O_4$, which was well matched with published JCPDS data (JCPDS 34-0425) [25]. In addition, the two characteristic peaks at 12.9° and 27.4° were observed for pure g-C_3N_4, with the former (100) plane diffraction peak being assigned to the periodic array of in-planar tri-s-triazine whereas the later (002) plane diffraction peak was attributed to the inter planar stacking of the conjugated aromatic system (JCPDS 87–1526) [26]. The

feature peaks of the g-C_3N_4 and $CuFe_2O_4$ phases coexisted within the $CuFe_2O_4$/g-C_3N_4 hybrids, which indicated that the $CuFe_2O_4$ was successfully loaded onto the g-C_3N_4. The intensity of the (002) diffraction peak of g-C_3N_4 was gradually increased with its higher content in the $CuFe_2O_4$/g-C_3N_4 hybrids.

The FT-IR spectra of g-C_3N_4, $CuFe_2O_4$, and the series of $CuFe_2O_4$/g-C_3N_4 hybrids with different g-C_3N_4 content levels are depicted in Fig. 1b. For the pure g-C_3N_4, the peaks at 1201, 1313, 1394, 1537, and 1626 cm^{-1} were derived from the skeletal stretching of C−N heterocycles comprising either the stretching vibrations of trigonal C−N(−C)−C or bridging C−NH−C units [27]. The intensive peak at 802 cm^{-1} was attributed to the vibration of the triazine units [28]. The absorption band at 572 cm^{-1} was derived from the formation of the Fe−O bond within the tetrahedral FeO_6 groups of the spinel-type compounds [24,25]. Moreover, all the characteristic peaks of g-C_3N_4 and $CuFe_2O_4$ were presented in the $CuFe_2O_4$/g-C_3N_4 photocatalyst, which indicated the successful synthesis of the two semiconductors. It could be observed that the intensities of the g-C_3N_4 diffraction peaks gradually became stronger with the decreased $CuFe_2O_4$ contents.

The morphologies and microstructures of the as-synthesized g-C_3N_4 and $CuFe_2O_4$/g-C_3N_4 hybrids were verified by FESEM (Fig. S2 and Fig. 2a) and FETEM images (Fig. 2b–d). Fig. S2 depicts the layered structure of pure g-C_3N_4 and Fig. 2a shows that the layered structures of the pristine g-C_3N_4 samples were well interwoven within the binary composite to form a p-n heterojunction, which facilitated photogenerated carrier transfer to enhance the photocatalytic performance. As can be seen from Fig. 2b–d, the $CuFe_2O_4$ (tens of nanometers) were well encapsulated within the g-C_3N_4 film (several nanometers). The interfaces between g-C_3N_4 and $CuFe_2O_4$ were intimate, which further confirmed the formation of $CuFe_2O_4$/g-C_3N_4 heterojunctions. Meanwhile, the lattice fringes with a spacing of 0.236 nm corresponding to the (311) plane of $CuFe_2O_4$ was consistent with the XRD results. Furthermore, EDS mapping analyses (Fig. 2e–j) revealed the uniform distribution of five elements (C, N, O, Cu, and Fe) throughout the catalyst. The g-C_3N_4 coupled with $CuFe_2O_4$ facilitated charge transfer between their surfaces, which enhanced the separation of photogenerated charges [29].

3.2. Chemical state analysis

X-ray photoelectron spectroscopy (XPS) measurements were carried out to elucidate the surface electronic states of the as-prepared g-C_3N_4/$CuFe_2O_4$ samples (Fig. 3). The survey XPS spectrum (Fig. 3a) of the g-C_3N_4/$CuFe_2O_4$ composite displays the coexistence of C, N, O, Fe, and Cu elements. The high resolution C1 s spectrum (Fig. 3b) was fitted into two peaks at 284.6 and 288.4 eV. The first peak was attributed to sp2 carbon in the g-C_3N_4 and benzoic rings. The second peak was assigned to sp2 hybridized carbon in the N-containing aromatic ring (N−C=N) [30]. In the high resolution O1 s spectrum (Fig. 3d), the two peaks with
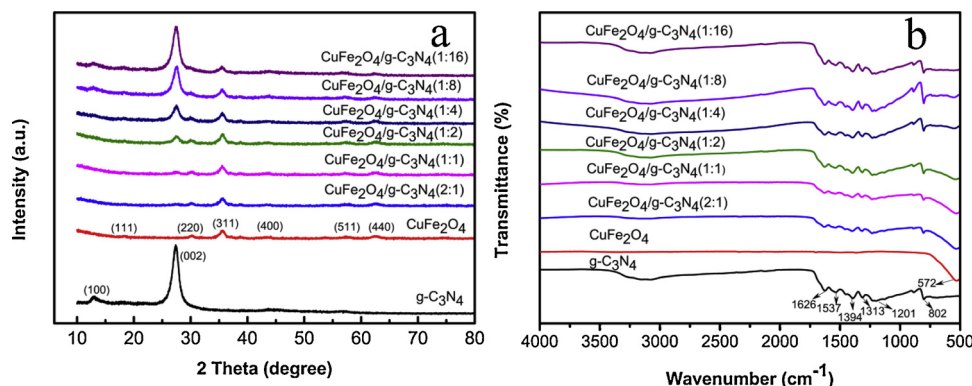

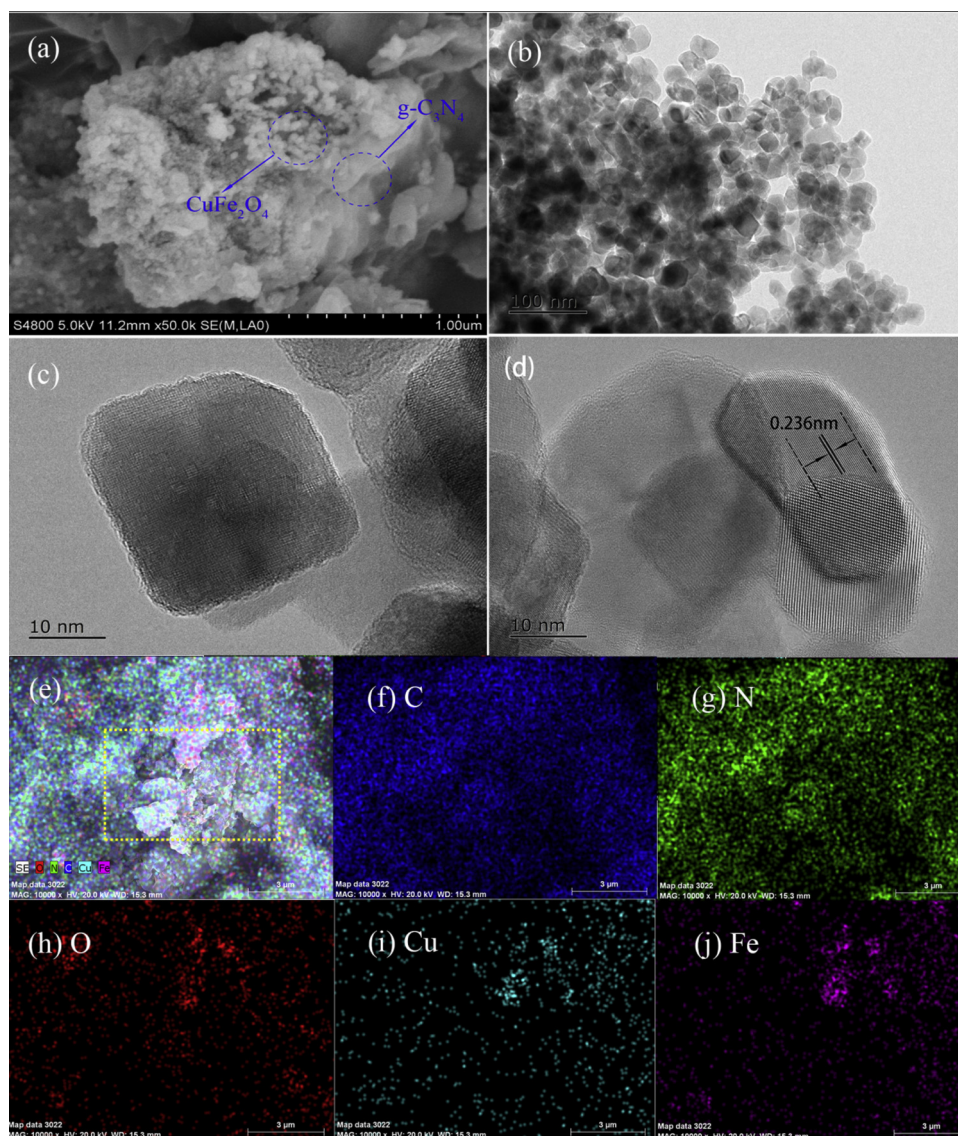**Fig. 1.** (a) XRD pattern; (b) FT-IR pattern of the samples.

Fig. 2. (a) SEM image; (b)-(d) TEM image; (e)-(j) EDS elemental mapping images of (1:8) CuFe$_2$O$_4$/g-C$_3$N$_4$ composite.

binding energies of 529.5 and 531.1 eV could be ascribed to the lattice oxide oxygen of metal oxides (Fe-O and Cu-O), and the adsorption of hydroxyl groups on the surface [31]. The N1 s XPS spectra (Fig. 3c) could be deconvoluted into two peaks at 398.4 and 399.8 eV, with the first peak being attributed to the sp2 hybridized aromatic nitrogen bonded to carbon atoms (C=N−C), and the second peak being assigned to the tertiary nitrogen (N-C$_3$) [32]. For the Fe 2p spectra (Fig. 3e), five fitted peaks were observed at 710.1, 712.0, 718.2, 723.5 and 725.1 eV, respectively. The peak at 710.1 eV could be attributed to the binding energies of $2p_{3/2}$ for Fe^{3+} [33,34]. The peaks at 712.0 and 723.5 eV were associated with the $2p_{3/2}$ and $2p_{1/2}$ of the Fe^{2+} [35]. The peak at 725.1 eV was assigned to the binding energies of $2p_{1/2}$ of Fe^{2+} and Fe^{3+} [36]. The peak at 718.2 eV was a satellite for the above four peaks, which indicated that Fe^{2+} and Fe^{3+} coexist in the catalyst. For the XPS of the Cu 2p regions, the peak located at 932.9 eV was ascribed to the Cu (I) species. The Cu $2p_{3/2}$ peak at 934.0 eV and its shakeup satellites were associated with Cu (II) [37]. The peak appearing at 952.8 eV with a satellite at 961.6 eV were assigned to Cu $2p_{1/2}$ (Fig. 3f) [38].

3.3. Photoelectrochemical and optical properties

The optical properties of the as-synthesized photocatalysts were investigated by UV–vis/DRS, with the results of the g-C$_3$N$_4$, CuFe$_2$O$_4$, and (1:8) CuFe$_2$O$_4$/g-C$_3$N$_4$ composites depicted in Fig. 4a. The absorption threshold value of the (1:8)CuFe$_2$O$_4$/g-C$_3$N$_4$ was extended up to the broader visible light region, and the primary adsorption edge of the pure g-C$_3$N$_4$ appeared at 450 nm. The band gap energies of the direct transition semiconductor could be calculated by a plot of (ahv)^2 versus the photo energy (hv) based on the Kubelka–Munk function [39]. Thus, the band gaps of the as-prepared g-C$_3$N$_4$ and CuFe$_2$O$_4$ were estimated to be 2.72 and 1.33 eV (Fig. 4b), respectively.

Photoluminescence (PL) analysis was performed to investigate the electron-hole separation efficiency under the Vis/g-C$_3$N$_4$/CuFe$_2$O$_4$/PDS system. The PL spectra of the g-C$_3$N$_4$ and g-C$_3$N$_4$/CuFe$_2$O$_4$ composites were shown in Fig. 5a. A weaker emission peak intensity represented a lower recombination possibility of photoinduced charge carriers due to the PL emission that resulted from the recombination of photoexcited electrons and holes [40]. The peak intensity of the g-C$_3$N$_4$/CuFe$_2$O$_4$ composite was weaker than g-C$_3$N$_4$, which suggested an inhibited recombination rate of the photoinduced electrons and holes. It was concluded that the g-C$_3$N$_4$/CuFe$_2$O$_4$ composites exhibited higher photocatalytic activity.

To further illustrate the above results, the electron transfer performance and photogenerated charge separation were evaluated through
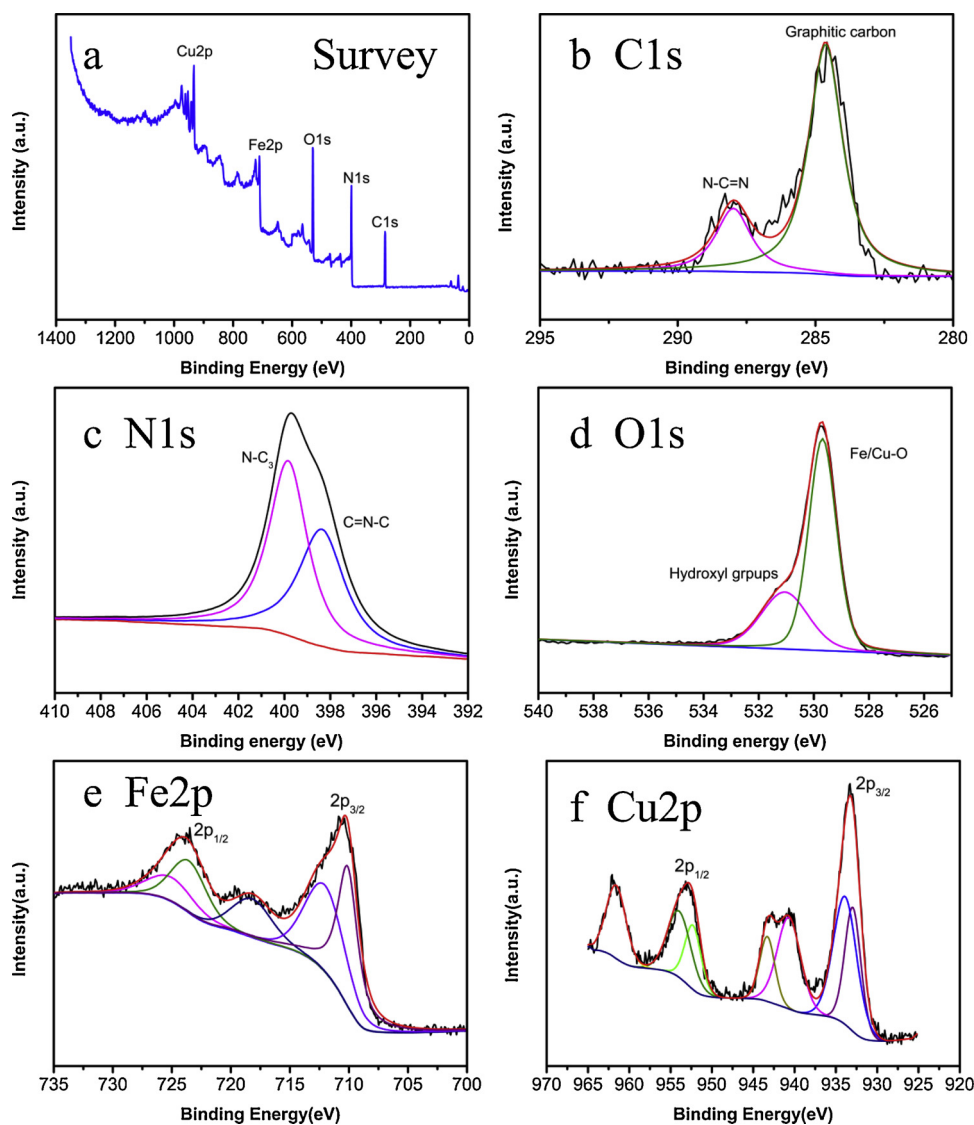
Fig. 3. (a) XPS survey; (b) C 1 s spectra; (c) N 1 s spectra; (d) O 1 s spectra; (e) Fe 2p spectra; (f) Cu 2p spectra of (1:8) $CuFe_2O_4/g\text{-}C_3N_4$.

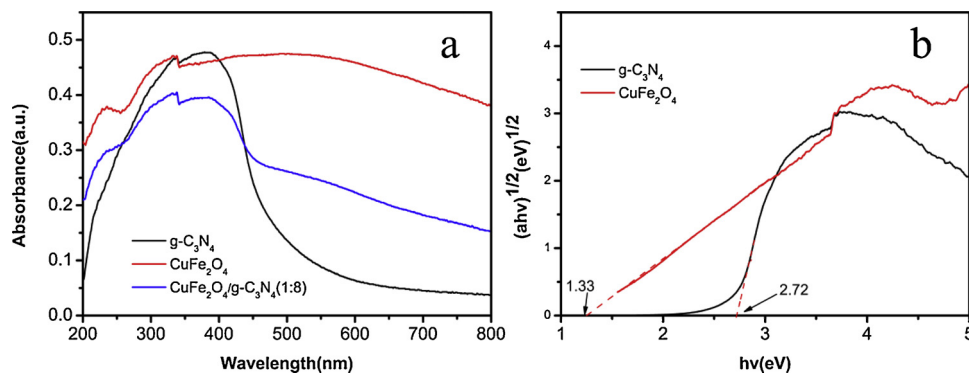**Fig. 4.** (a) UV–vis DRS spectra; (b) Plot of $(\alpha h\nu)^2$ vs. photo energy ($h\nu$) for the band gap energy of $g\text{-}C_3N_4$ and $CuFe_2O_4$ samples.

the analysis of the transient photocurrent and electrochemical impedance spectroscopy (EIS) experiments. A sensitive photoelectric response was observed for each on off cycle in the $g\text{-}C_3N_4$ and $g\text{-}C_3N_4/$ $CuFe_2O_4$ composites (Fig. 5b). The photocurrents for the $g\text{-}C_3N_4/$ $CuFe_2O_4$ composite exhibited an obvious enhancement in contrast to the $g\text{-}C_3N_4$, which suggested that the $g\text{-}C_3N_4/CuFe_2O_4$ composite had a lower recombination efficiency of photoinduced electron-hole pairs

[41]. Fig. 5c shows Nyquist impedance plots of the $g\text{-}C_3N_4$, $CuFe_2O_4$, $g\text{-}C_3N_4/CuFe_2O_4$ composites and $g\text{-}C_3N_4/CuFe_2O_4/PDS$. It was established that the smaller arc in the EIS Nyquist plot exhibited a lower charge-transfer resistance on the surface of the electrode [42]. The $g\text{-}C_3N_4/CuFe_2O_4$ composite with PDS possessed a smaller arc radius on the EIS Nyquist plot than the bare $g\text{-}C_3N_4$, $CuFe_2O_4$ and $g\text{-}C_3N_4/$ $CuFe_2O_4$ composites, which meant that the $g\text{-}C_3N_4/CuFe_2O_4$ composite
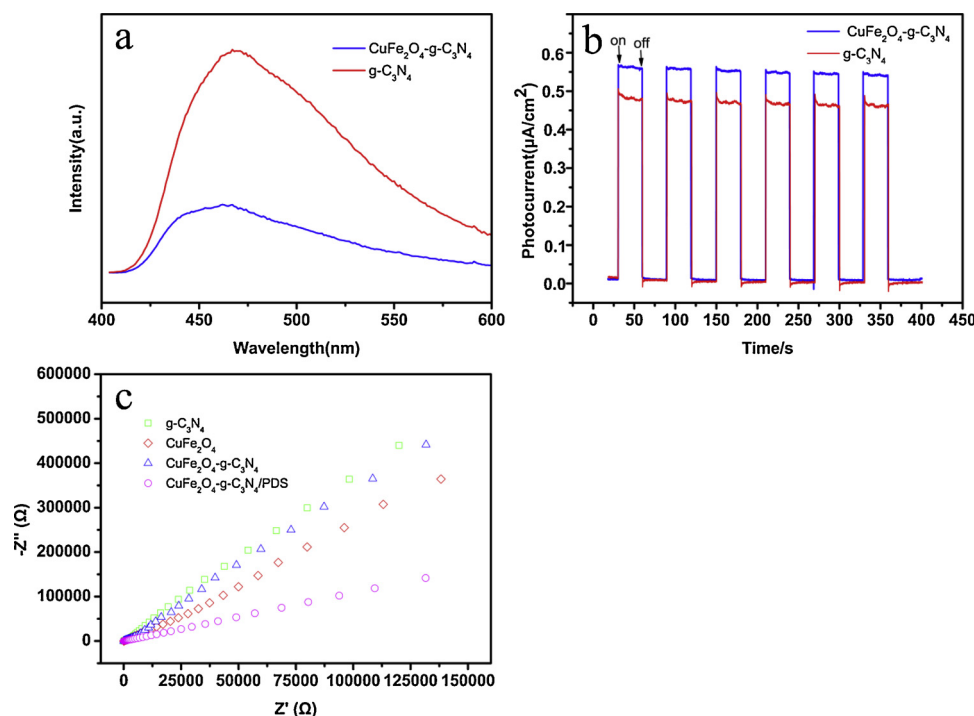
Fig. 5. (a) PL spectra; (b) transient photocurrent responses; (c) EIS Nyquist plots.

with PDS could enhance the migration and separation of photoexcited charge carriers.

3.4. Photocatalytic activity

The photocatalytic performance of the prepared catalysts was investigated via the degradation of PRO under visible light irradiation. As shown in Fig. 6a and Fig. S3, the addition of PDS, g-C_3N_4, and $CuFe_2O_4$ alone was found to result in only a slight degradation of PRO, where 15.7%, 16.7%, and 13.8% removal efficiencies were achieved, respectively. In contrast, the PDS served as an electron acceptor when combined with g-C_3N_4 and $CuFe_2O_4$, which resulted in obvious improvements toward the degradation of PRO, where 33.9% and 39.5% removal efficiencies were obtained in the g-C_3N_4/PDS and $CuFe_2O_4$/ PDS systems, respectively. As compared to a single catalyst, the g-C_3N_4/ $CuFe_2O_4$ heterojunction exhibited excellent photocatalytic activity,
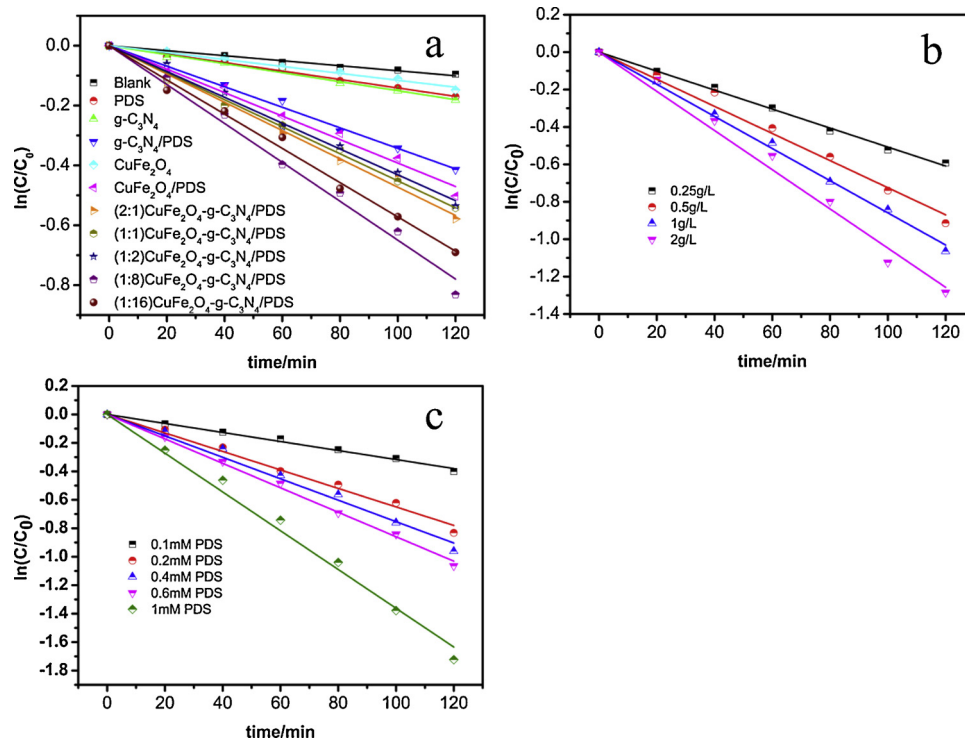

Fig. 6. (a) The degradation of PRO under various photocatalytic processes (catalysts = 1 g L^{-1}, [PDS] = 0.2 mM); (b) Effects of photocatalyst quantity; (c) Effects of PDS concentration. (Experimental conditions: [PRO] = 0.02 mM, pH = 6.4.).

which implied a potent synergistic effect within the composites. Compared to samples with different CuFe$_2$O$_4$ content, it was observed that (1:8) CuFe$_2$O$_4$/g-C$_3$N$_4$ demonstrated optimal photocatalytic activity among these heterojunction photocatalysts, where 56.5% of PRO was removed within 120 min with the (1:8) CuFe$_2$O$_4$/g-C$_3$N$_4$ /PDS/Vis system.

Several experiments under various conditions were carried out to evaluate the degradation of PRO. Fig. 6b–c reveals the effects of major factors in terms of the quantity of photocatalyst and PDS concentration on the degradation of PRO under the g-C$_3$N$_4$/CuFe$_2$O$_4$/PDS/Vis process. As shown in Fig. 6b, An increase in the photocatalyst dosage in the range from 0.25 to 2 g L^{-1}, gradually enhanced the degradation of PRO. This may have been attributed to the additional electrons and holes that were generated due to the photoexcitation of g-C$_3$N$_4$/ CuFe$_2$O$_4$ upon visible light irradiation. The increased photocatalyst dosage induced the capture photogenerated electrons to increase the generation of reactive radicals.

The quantity of reactive radicals (SO$_4^{\cdot-}$ and $\cdot$OH) increased with higher PDS concentrations, thus accelerating the photocatalytic performance. There was a significant enhancement in the degradation of PRO when increasing the concentration of PDS from 0.1 to 0.2 mM. The degradation of PRO was only slightly accelerated when the concentration of PDS was increased to 0.6 mM. This may have been because the photogenerated electrons were not effective enough to activate the PDS at a relatively higher concentration. It was also observed that the scavenging of SO$_4^{\cdot-}$ radicals would cause an effect at higher PDS concentrations, as described by the following Eq. (1):

$$SO_4^{\cdot-} + S_2O_8^{2-} \rightarrow S_2O_8^- + SO_4^{2-} \tag{1}$$

The degradation efficiency of PRO increased remarkably to 82.2% when the PDS continually increased up to 1 mM due to the sustained formation of SO$_4^{\cdot-}$ overcome the scavenging effects.

3.5. Photocatalytic mechanism

Reactive species quenching experiments were conducted to elucidate the mechanism of photocatalytic process. Fig. 7a depicts the effects of different scavengers on the degradation efficiency of PRO under the Vis/CuFe$_2$O$_4$/g-C$_3$N$_4$/PDS system. Reactive species were observed to play an important role when the inhibition of the degradation efficiency of PRO was increased. It was clear that the PRO degradation rate was significantly inhibited by a O$_2^{\cdot-}$ scavenger; when p-BQ [43] was added, which identified that O$_2^{\cdot-}$ was the primary reactive species. This may have been due to the O$_2$ adsorbed on the surface of the photocatalyst reacting with photogenerated e$^-$ to produce O$_2^{\cdot-}$. The addition of K$_2$Cr$_2$O$_7$ obviously decreased the degradation of PRO, which suggested that e$^-$ played an important role. The PDS served as electrons acceptor and induced by CuFe$_2$O$_4$ to produce SO$_4^{\cdot-}$, which was confirmed by its decreased efficiency with the introduction of TBA (SO$_4^{\cdot-}$ scavenger). There were conspicuous changes in the PRO degradation rate when EtOH ($\cdot$OH and SO$_4^{\cdot-}$ scavenger) [44,45] was added. This revealed that $\cdot$OH was the reactive species responsible for the reaction coexisting with SO$_4^{\cdot-}$. The presence of Na$_2$C$_2$O$_4$ inhibited the reaction to some extent, which indicated the h$^+$ was also involved in the photocatalytic PRO oxidation process.

ESR measurements were employed to further validate the ROS in the Vis/CuFe$_2$O$_4$/g-C$_3$N$_4$/PDS system using 5,5-Dimethyl-1-pyrroline N-oxide (DMPO) and 4-oxo-2,2,6,6-tetramethylpiperidine (TEMP) as radical spin trapping agent [46–48]. As shown in Fig. 7b, the intensities of the DMPO-O$_2^{\cdot-}$ adducts become stronger upon visible light irradiation, which suggested that O$_2^{\bullet-}$ played a significant role in the photocatalytic process. Fig. 7c shows that the DMPO-$\cdot$OH and DMPO-SO$_4^{\cdot-}$ adducts coexisted with increasing trends compared to a dark condition. Furthermore, the role of ^{1}O$_2$ was also assessed in the reaction; the intensities of the peaks of the spin-trapped TEMP-^{1}O$_2$ increased from 0 to 10 min (Fig. 7d). Therefore, the quenching experiments and ESR analysis revealed that the combined effects of O$_2^{\cdot-}$, ^{1}O$_2$, h$^+$, $\cdot$OH, and SO$_4^{\cdot-}$ were responsible for the photocatalytic process. The synergetic effects proceeded within g-C$_3$N$_4$ and CuFe$_2$O$_4$ via p-n heterojunction interfacial structures, which were beneficial to harvest of visible light and the separation of charge carriers. The introduction of PDS as electron acceptor led to the generation of additional active species, which further improved the photocatalytic activity for the degradation of PRO.

According to the above results, a possible photocatalytic mechanism for the degradation of PRO under g-C$_3$N$_4$/CuFe$_2$O$_4$/PDS/Vis system was proposed (Scheme 1). Owing to the modification of CuFe$_2$O$_4$, the harvesting ability of visible light and the separation of photogenerated
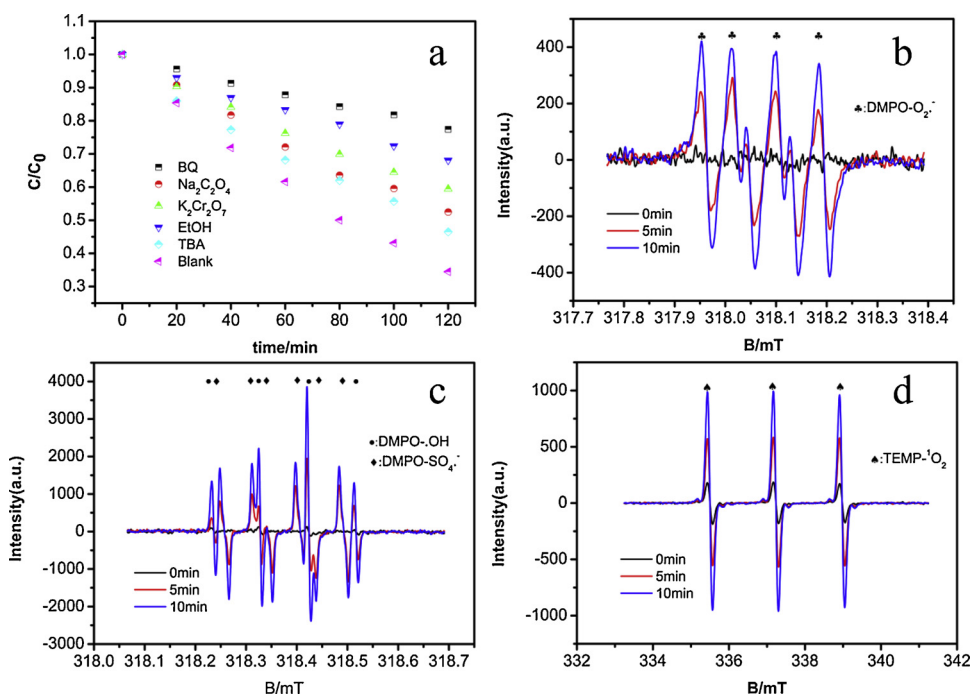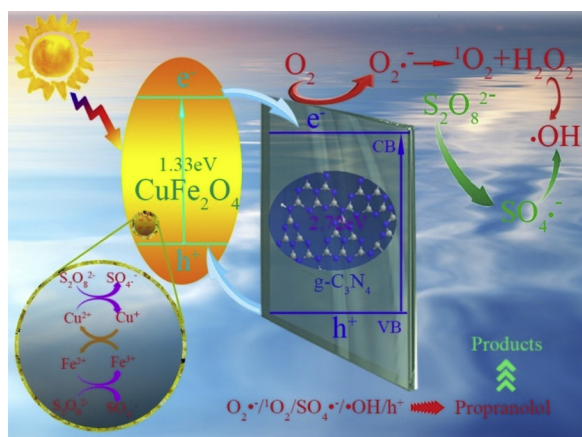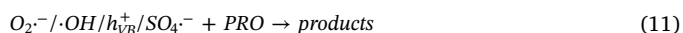

Fig. 7. (a) Effects of the addition of reactive species scavengers; (b) DMPO-$\bullet$OH and DMPO-SO$_4^{\cdot-}$ adducts; (c) DMPO-O$_2^{\cdot-}$ adducts; (d) TEMP-^{1}O$_2$ under visible light irradiation. (Experimental conditions: g-C$_3$N$_4$/CuFe$_2$O$_4$ = 1 g L^{-1}, [PDS] = 0.6 mM, initial pH = 6.4, [DMPO] = 20 mM, [TEMP] = 20 mM.).

Scheme 1. Mechanism for propranolol degradation in the g-C₃N₄/CuFe₂O₄/PDS/Vis system.

charge carriers were improved, which suggested that the generation of additional photoexcited electrons and holes (Eq. (2)). Moreover, the e^- captured by PDS produced $SO_4{}^{\cdot-}$, which further inhibited the recombination of electrons and holes. The valence bands (VB) of the CuFe₂O₄ and g-C₃N₄ were found to be 0.23 eV and 1.80 eV (Fig. S4) using the XPS technique. The holes generated in the VB of g-C₃N₄ could migrate to CuFe₂O₄ due to the VB level of g-C₃N₄ being more positive than CuFe₂O₄. But the generated holes could not oxidize the H₂O molecules adsorbed to the surface of the catalyst to form •OH, since the valence band potential of CuFe₂O₄ (0.23 eV vs. NHE) was more negative than the standard redox potential E^o(•OH/H₂O) (+ 2.7 eV vs. NHE). Hence, based on the band-gap results and the empirical formula of $Eg = E_{VB} - E_{CB}$, the conduction band of the CuFe₂O₄ and g-C₃N₄ was calculated to be -1.10 and -0.92 eV, respectively. The generated electrons in the CB of CuFe₂O₄ (-1.10 eV) could be transferred to the CB of g-C₃N₄ (-0.92 eV), which was more significantly negative than the standard redox potential E^o ($SO_4{}^{\cdot-}/S_2O_8{}^{2-}$) [49].This satisfied the thermodynamic requirements for the production of $SO_4{}^{\cdot-}$ radicals via the activation of PDS by e^- under visible light irradiation (Eq.(7)).

Further, Fe(II) and Cu (I) on the CuFe₂O₄ crystal surface could also activate PDS to generate $SO_4{}^{\cdot-}$ (Eqs. (9)–(10)). Subsequently, $SO_4{}^{\cdot-}$ reacted with H₂O or OH⁻ to form ·OH (Eq. (8)), which possessed the capacity to degrade PRO. Moreover, the E^o ($O_2/O_2{}^{\cdot-}$) (−0.33 eV vs. NHE) [50] was less negative than the conduction band of g-C₃N₄ (-0.92 eV), which meant that e^- could also react with O₂ to form $O_2{}^{\cdot-}$ (Eq. (3)). Furthermore, $O_2{}^{\cdot-}$ had the ability to transform to ¹O₂ and H₂O₂ (Eqs. (4)–(5)). Finally, the electrons can react with H₂O₂ to produce •OH (Eq. (6)). In summary, $O_2{}^{\cdot-}$, ¹O₂, h⁺, $SO_4{}^{\cdot-}$ and •OH contributed to the degradation of PRO under the Vis/g-C₃N₄/CuFe₂O₄/PDS system.

$$g-C_3N_4/CuFe_2O_4 \xrightarrow{hv} h_{VB}^+ + e_{CB}^- \tag{2}$$

$$O_2 + e^- \rightarrow O_2{}^{\cdot-} \tag{3}$$

$$O_2{}^{\cdot-} + H^+ \rightarrow HO_2\cdot \tag{4}$$

$$2HO_2\cdot \rightarrow H_2O_2 + {}^1O_2 \tag{5}$$

$$H_2O_2 + e^- \rightarrow \cdot OH + OH^- \tag{6}$$

$$S_2O_8{}^{2-} + e^- \rightarrow 2SO_4{}^{\cdot-} \tag{7}$$

$$SO_4{}^{\cdot-} + OH^- \rightarrow \cdot OH + SO_4{}^{2-} \tag{8}$$

$$\equiv Cu^I + S_2O_8{}^{2-} + e^- \rightarrow Cu^{II} + SO_4{}^{\cdot-} + SO_4{}^{2-} \tag{9}$$

$$\equiv Fe^{II} + S_2O_8{}^{2-} + e^- \rightarrow Fe^{III} + SO_4{}^{\cdot-} + SO_4{}^{2-} \tag{10}$$

$$O_2{}^{\cdot-}/\cdot OH/h_{VB}^+/SO_4{}^{\cdot-} + PRO \rightarrow products \tag{11}$$
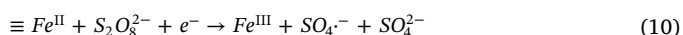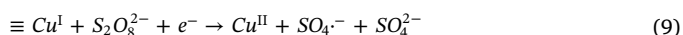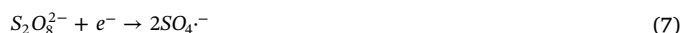
3.6. Transformation pathways

The g-C₃N₄/CuFe₂O₄ composite combined with PDS under visible light irradiation generated a series of transformation products. The transformation products were tentatively identified through the interpretation of MS/MS spectra and comparisons with those described in the previous literature. Table S4 summarizes the proposed structural compositions, *m/z* ratios and characteristic fragment ions [51–54], with the product ion mass spectra presented in Figs.S5a-5i. The potential
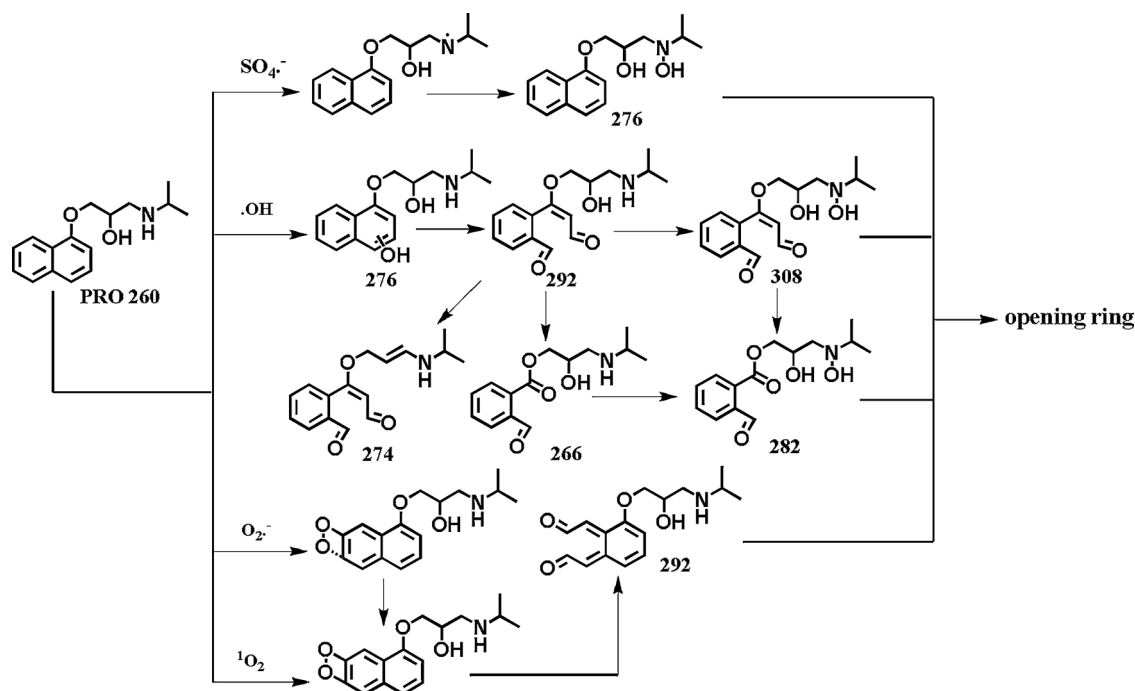
Fig. 8. Potential degradation pathways of PRO in the Vis/g-C₃N₄/CuFe₂O₄/PDS system.

degradation pathways of PRO under Vis/g-C$_3$N$_4$/CuFe$_2$O$_4$/PDS are illustrated in Fig. 8.

One proposed pathway was that SO$_4^{\cdot-}$ attacked PRO through electron transfer to generate N-centered radial cations, which further reacted with H$_2$O via hydroxyl abstraction or addition to form hydroxylated PRO (*m/z* 276). Ahmed et al. reported that the SO$_4$•$^-$-based oxidative transformation of diclofenac and sulfamethoxazole proceeded through similar mechanisms [55].

Another pathway was attributed to the electrophilic attack of the naphthalene ring by •OH (*m/z* 276). The *m/z* 276 gave rise to a further naphthalene ring-opening product (*m/z* 292), which has been frequently determined previously in other advanced oxidative process (AOP) [54,56]. On one hand, the *m/z* 292 was subsequently transformed to *m/z* 274 and *m/z* 266 through dehydration and decarboxylation, respectively; On the other hand, the *m/z* 308 was derived from *m/z* 292 via the attack of SO$_4^{\cdot-}$ or $\cdot$OH on the amino moiety. Finally, the *m/z* 282 arose via the decarboxylation of *m/z* 308 and the hydroxylation of *m/z* 266. As for the role of molecular oxygen, O$_2^{\cdot-}$ or ^{1}O$_2$, the ^{1}O$_2$ preferentially interacted with PRO to form endoperoxides, while O$_2^{\cdot-}$ was suggested to preferentially interact with PRO•$^+$ to generate a zwitterion or diradical due to its nucleophilic character [57]. Finally, the formation of endoperoxides and diradicals resulted in a common intermediate, *m/z* 292.

Based on the above discussions, the hydroxylation of a naphthalene ring, oxidation of a secondary amine moiety on the aliphatic chain, decarboxylation, and nucleophilic addition by molecular oxygen were the primary transformation pathways for the degradation of PRO under the Vis/g-C$_3$N$_4$/CuFe$_2$O$_4$/PDS system.

4. Conclusion

CuFe$_2$O$_4$ modified g-C$_3$N$_4$ heterojunction photocatalysts were successfully fabricated. The CuFe$_2$O$_4$ /g-C$_3$N$_4$ couple with PDS showed excellent photocatalytic performance for the degradation of PRO owing to the synergistic effects of the photocatalysis of CuFe$_2$O$_4$/g-C$_3$N$_4$ composite and the chemical activation of PDS. Photoelectrochemical tests demonstrated that the improved photocatalytic performance could be ascribed to the enhanced separation efficiency of photogenerated charge pairs, which accelerated the generation of reactive species. Quenching experiments and ESR analysis indicated that SO$_4^{\cdot-}$, $\cdot$OH, O$_2^{\cdot-}$, ^{1}O$_2$ and h$^+$ were the reactive oxidizing species responsible for the photocatalytic process. The PDS served as a photogenerated electron acceptor to form SO$_4$•$^-$ and the self-redox cycles of iron and copper in CuFe$_2$O$_4$ were responsible for the improved photocatalytic performance under the Vis/g-C$_3$N$_4$/CuFe$_2$O$_4$/PDS system. The transformation products were primarily derived from the $\cdot$OH, O$_2^{\cdot-}$ and ^{1}O$_2$ attack on the naphthalene group, and SO$_4^{\cdot-}$ attack on the secondary amine moiety.

Acknowledgments

Appendix A. Supplementary data

Supplementary material related to this article can be found, in the online version, at doi:https://doi.org/10.1016/j.apcatb.2018.12.043.

References

[1] V. Gabetgiraud, C. Miège, J.M. Choubert, S.M. Ruel, M. Coquery, Sci. Total Environ. 408 (2010) 4257–4269.
[2] B. Petrie, B. Barden, B. Kasprzykhordern, Water Res. 72 (2015) 3–27.
[3] D.B. Huggett, B.W. Brooks, B. Peterson, C.M. Foran, D. Schlenk, Arch. Environ. Contam. Toxicol. 43 (2002) 229–235.
[4] K. Fent, A.A. Weston, D. Caminada, Aquat. Toxicol. 76 (2006) 122.
[5] Y. He, B. Jiang, Y. Jiang, J. Chen, Y.X. Zhang, J. Hazard. Mater. 344 (2018) 230–240.
[6] K. Ilho, N. Yamashita, H. Tanaka, Chemosphere 77 (2009) 518–525.
[7] E. Isarainchávez, P.L. Cabot, F. Centellas, R.M. Rodríguez, C. Arias, J.A. Garrido, E. Brillas, J. Hazard. Mater. 185 (2011) 1228–1235.
[8] I.H. Kim, N. Yamashita, Y. Kato, H. Tanaka, Water Sci. Technol. 59 (2009) 945–955.
[9] F. Dong, T. Xiong, Y. Sun, L. Lu, Y. Zhang, H. Zhang, H. Huang, Y. Zhou, Z. Wu, Appl. Catal. B 219 (2017) 450–458.
[10] G. Liu, P. Niu, C. Sun, S.C. Smith, Z. Chen, G.Q. Lu, H.M. Cheng, J. Am. Chem. Soc. 132 (2010) 11642–11648.
[11] S. Cao, J. Low, J. Yu, M. Jaroniec, Cheminform 27 (2015) 2150–2176.
[12] W. Wan, S. Yu, F. Dong, Q. Zhang, Y. Zhou, J. Mater. Chem. 4 (2016) 7823–7829.
[13] R. Zhang, M. Ma, Q. Zhang, F. Dong, Y. Zhou, Appl. Catal. B 235 (2018) 17–25.
[14] W.K. Jo, T.S. Natarajan, Chem. Eng. J. 281 (2015) 549–565.
[15] X. Dai, M. Xie, S. Meng, X. Fu, S. Chen, Appl. Catal., B s 158–159 (2014) 382–390.
[16] Y. He, Y. Wang, L. Zhang, B. Teng, M. Fan, Appl. Catal. B 168-169 (2015) 1–8.
[17] L. Cui, X. Ding, Y. Wang, H. Shi, L. Huang, Y. Zuo, S. Kang, Appl. Surf. Sci. 391 (2016) 202–210.
[18] D. Yuan, L. Huang, Y. Li, Y. Xu, X. Hui, S. Huang, J. Yan, M. He, H. Li, RSC Adv. 6 (2016) 41204–41213.
[19] M. Chen, J. Yao, Y. Huang, H. Gong, W. Chu, Chem. Eng. J. 334 (2018) 453–461.
[20] W. Zhang, B. Quan, C. Lee, S.K. Park, X. Li, E. Choi, G. Diao, Y. Piao, ACS Appl. Mater. Interfaces 7 (2015) 2404–2414.
[21] Y. Zhao, G. He, W. Dai, H. Chen, Ind. Eng. Chem. Res. 53 (2014) 12566–12574.
[22] L.W. Matzek, K.E. Carter, Chemosphere 151 (2016) 178.
[23] X. Wang, K. Maeda, A. Thomas, K. Takanabe, G. Xin, J.M. Carlsson, K. Domen, M. Antonietti, A metal-free polymeric photocatalyst for hydrogen production from water under visible light.
[24] Y. Ding, L. Zhu, N. Wang, H. Tang, Appl. Catal. B 129 (2013) 153–162.
[25] P. Laokul, V. Amornkitbamrung, S. Seraphin, S. Maensiri, Curr. Appl. Phys. 11 (2011) 101–108.
[26] K. Vignesh, A. Suganthi, B.K. Min, M. Kang, J. Mol. Catal. A Chem. 395 (2014) 373–383.
[27] T.Y. Ma, T. Tang, S. Dai, S.Z. Qiao, Small 10 (2014) 2382–2389.
[28] P. Niu, L. Zhang, G. Liu, H.M. Cheng, Adv. Funct. Mater. 22 (2012) 4763–4770.
[29] W.K. Jo, S.S.N. Clament, J. Hazard. Mater. 299 (2015) 462–470.
[30] A. Thomas, A. Fischer, F. Goettmann, M. Antonietti, J.O. Mueller, R. Schloegl, J.M. Carlsson, Cheminform 40 (2009) 4893–4908.
[31] Q. Fei, C. Wei, B. Xu, Chem. Eng. J. 262 (2015) 552–562.
[32] R. Cheng, X. Fan, M. Wang, M. Li, J. Tian, L. Zhang, RSC Adv. 6 (2016) 18990–18995.
[33] Y. Hou, X.-Y. Li, Q.-D. Zhao, X. Quan, G.-H. Chen, Adv. Funct. Mater. 20 (2010) 2165–2174.
[34] X. Qian, M. Ren, Y. Zhu, D. Yue, Y. Han, J. Jia, Y. Zhao, Environ. Sci. Technol. 51 (2017) 3993–4000.
[35] H. Peng, Z. Mo, S. Liao, H. Liang, L. Yang, F. Luo, H. Song, Y. Zhong, B. Zhang, Sci. Rep. 3 (2013) 1765.
[36] Y. Su, H. Jiang, Y. Zhu, X. Yang, J. Shen, W. Zou, J. Chen, C. Li, J. Mater. Chem. 2 (2014) 7281–7287.
[37] J. Fan, Y. Dai, Y. Li, N. Zheng, J. Guo, X. Yan, G.D. Stucky, J. Am. Chem. Soc. 131 (2009) 15568–15569.
[38] Y. Yao, F. Lu, Y. Zhu, F. Wei, X. Liu, C. Lian, S. Wang, J. Hazard. Mater. 297 (2015) 224.
[39] Y. Yao, Y. Cai, F. Lu, J. Qin, F. Wei, C. Xu, S. Wang, Ind. Eng. Chem. Res. 53 (2015) 17294–17302.
[40] Y. Yang, J. Wen, J. Wei, R. Xiong, J. Shi, C. Pan, ACS Appl. Mater. Interfaces 5 (2013) 6201–6207.
[41] H. Shao, X. Zhao, Y. Wang, R. Mao, Y. Wang, M. Qiao, Y. Zhu, Appl. Catal. B 218 (2017).
[42] W. Xu, C. Zheng, H. Hua, Q. Yang, L. Chen, Y. Xi, C. Hu, Appl. Surf. Sci. 327 (2015) 140–148.
[43] X. Wu, X. Gu, S. Lu, M. Xu, X. Zang, Z. Miao, Z. Qiu, S. Qian, Chem. Eng. J. 255 (2014) 585–592.
[44] G.V. Buxton, C.L. Greenstock, W.P. Helman, A.B. Ross, J. Phys. Chem. Ref. Data 17 (1988) 513–886.
[45] P. Neta, R.E. Huie, A.B. Ross, J. Phys. Chem. Ref. Data 17 (1988) 1027–1284.
[46] P. Chen, F. Wang, Z.F. Chen, Q. Zhang, Y. Su, L. Shen, K. Yao, Y. Liu, Z. Cai, W. Lv, Appl. Catal. B 204 (2017) 250–259.
[47] P. Chen, F. Wang, Q. Zhang, Y. Su, L. Shen, K. Yao, Z.F. Chen, Y. Liu, Z. Cai, W. Lv, Chemosphere 172 (2017) 193.
[48] H. Wang, Y. Sun, G. Jiang, Y. Zhang, H. Huang, Z. Wu, S.C. Lee, F. Dong, Environ. Sci. Technol. 52 (2018) 1479–1487.
[49] G. Zhou, H. Sun, S. Wang, H.M. Ang, M.O. Tadé, Sep. Purif. Technol. 80 (2011) 626–634.
[50] X. Li, J. Yu, M. Jaroniec, Chem. Soc. Rev. 45 (2016) 2603–2636.
[51] S.O. Ganiyu, N. Oturan, S. Raffy, G. Esposito, E.D.V. Hullebusch, M. Cretin, M.A. Oturan, Electrochim. Acta (2017).
[52] J. Santiago-Morales, A. Agüera, M.D.M. Gómez, A.R. Fernández-Alba, J. Giménez, S. Esplugas, R. Rosal, Appl. Catal. B 129 (2013) 13–29.
[53] M.L. Wilde, W.M. Mahmoud, K. Kümmerer, A.F. Martins, Sci. Total Environ. s 452–453 (2013) 137–147.
[54] Y.Q. Gao, N.Y. Gao, D.Q. Yin, F.X. Tian, Q.F. Zheng, Chemosphere 201 (2018) 50–58.
[55] M.M. Ahmed, S. Barbati, P. Doumenq, S. Chiron, Chem. Eng. J. 197 (2012) 440–447.
[56] G.A.K. Anquandah, V.K. Sharma, V.R. Panditi, P.R. Gardinali, H. Kim, M.A. Oturan, Chemosphere 91 (2013) 105–109.
[57] H.S. Wahab, T. Bredow, S.M. Aliwi, Surf. Sci. 603 (2009) 664–669.